

Article

Integrated Au/TiO₂ Nanostructured Photoanodes for Photoelectrochemical Organics Degradation

Roberto Matarrese ^{1,*}, Michele Mascia ², Annalisa Vacca ², Laura Mais ², Elisabetta M. Usai ², Matteo Ghidelli ^{3,4}, Luca Mascaretti ^{3,5}, Beatrice R. Bricchi ³, Valeria Russo ^{3,6}, Carlo S. Casari ^{3,6}, Andrea Li Bassi ^{3,6}, Isabella Nova ¹ and Simonetta Palmas ^{2,*}

¹ Dipartimento di Energia, Laboratorio di Catalisi e Processi Catalitici, Politecnico di Milano, via La Masa 34, I-20156 Milano, Italy; isabella.nova@polimi.it

² Università degli studi di Cagliari, Dipartimento di Ingegneria Meccanica, Chimica e dei Materiali, via Marengo 2, 09123 Cagliari, Italy; michele.mascia@unica.it (M.M.); annalisa.vacca@dimcm.unica.it (A.V.); l.mais@dimcm.unica.it (L.M.); elisabetta.usai@unica.it (E.M.U.)

³ Dipartimento di Energia, Laboratorio Materiali Micro e Nanostrutturati, Politecnico di Milano, via Ponzio 34/3, I-20133 Milano, Italy; m.ghidelli@mpie.de (M.G.); luca.mascaretti@upol.cz (L.M.); beatriceroberta.bricchi@polimi.it (B.R.B.); valeria.russo@polimi.it (V.R.); carlo.casari@polimi.it (C.S.C.); andrea.libassi@polimi.it (A.L.B.)

⁴ Department of Structure and Nano/-Micromechanics of Materials, Max-Planck-Institut für Eisenforschung GmbH, Max-Planck-straße 1, 40237 Düsseldorf, Germany

⁵ Regional Centre of Advanced Technologies and Materials, Faculty of Science, Palacký University Olomouc, Šlechtitelů 27, 783 71 Olomouc, Czech Republic

⁶ Center for Nanoscience and Technology – IIT@Polimi, via Giovanni Pascoli 70/3, 20133 Milano, Italy

* Correspondence: roberto.matarrese@polimi.it (R.M.); simonetta.palmas@dimcm.unica.it (S.P.)

Received: 7 March 2019; Accepted: 2 April 2019; Published: 5 April 2019



Abstract: In this work, hierarchical Au/TiO₂ nanostructures were studied as possible photoanodes for water splitting and bisphenol A (BPA) oxidation. TiO₂ samples were synthesized by Pulsed Laser Deposition (PLD), while Au nanoparticles (NPs) were differently dispersed (i.e., NPs at the bottom or at the top of the TiO₂, as well as integrated TiO₂/Au-NPs assemblies). Voltammetric scans and electrochemical impedance spectroscopy analysis were used to correlate the morphology of samples with their electrochemical properties; the working mechanism was investigated in the dark and in the presence of a light radiation, under neutral pH conditions towards the possible oxidation of both bisphenol A (BPA) and water molecules. Different behavior of the samples was observed, which may be attributed mainly to the distributions of Au NPs and to their dimension as well. In particular, the presence of NPs at the bottom seems to be the crucial point for the working mechanism of the structure, thanks to scattering effects that likely allow to better exploit the radiation.

Keywords: photoelectrocatalysis; TiO₂ nanostructures; Au nanoparticles; water splitting; bisphenol A oxidation

1. Introduction

This work focuses on two very important aspects in the field of photoelectrocatalysis: on one side, the synthesis of efficient photocatalysts to be used in a wide range of wavelengths (e.g., also under solar radiation), and on the other side the development of effective methods for the purification of industrial and domestic wastewater, with particular attention to those substances dangerous to human health that are not easily degradable by conventional methods. Among the others, bisphenol A (2,2-bis(4-hydroxyphenyl) propane or BPA), which is composed of two phenol molecules bonded by a methyl bridge and two methyl groups, deserves attention. This compound is used as an intermediate

(binding, plasticizing, and hardening) in plastics, paints/lacquers, binding materials, and filling materials, as well as an additive for flame-retardants, brake fluids, and thermal papers [1]. However, the most important field of usage of this compound is represented by polycarbonates and epoxy resins, that determined a huge increasing in the BPA demand, in the last few years: the global demand, which was 5.0 million tons in 2010 and 8 million tons in 2016, is projected to reach 10.6 million tons by 2022 [2]. As a result, BPA has been frequently detected in water and soil and its impact on both environment and human health is a major point of concern [2–5]. Accordingly, the removal of BPA from wastewater has become a priority for the scientific community and several methods for its degradation have been proposed in the literature (e.g., biological [6,7], catalytic [8], photocatalytic [9–11], and photoelectrocatalytic methods [12,13]), most of which reported high yields, up to 90–100%, at least in terms of BPA removal. However, the high number of papers that are still present in the recent literature indicate that the problem is far from resolved and a lot of interest still remains in finding effective and competitive methods for BPA degradation [14–17].

Focusing on photoelectrocatalytic processes, the present work proposes the use of nanostructured TiO₂ electrodes integrated with Au nanoparticles (NPs), and it investigates their electrochemical behavior during electrolysis both in KNO₃ solution and in the presence of BPA.

For a long time, our research group investigated nanostructured TiO₂ materials for photoelectrocatalytic applications [18–21], mostly facing the well-known major problems of TiO₂ which are the low quantum efficiency and the poor activation by visible light (i.e., solar light). More recently, some of us proposed the use of Pulsed Laser Deposition (PLD) for the synthesis of plasmonic Au NPs and their integration in hierarchical TiO₂ nanostructures [22], which have been preliminarily tested for the photodegradation of methyl orange under simulated natural sunlight [23]. Indeed, the use of hierarchical 3D nanostructures, with high roughness, can promote light absorption due the scattering effect over a large angular range. However, such an effect is not always exploitable, for example in the case of thin-film cells where the surface roughness would exceed the film thickness, and because the greater surface area increases minority carrier recombination in the surface and junction regions. Particularly, in these cases, the use of metallic nanostructures that support surface plasmons, could be effective [24]. For a given photoelectrode, various plasmonic mechanisms may be exploited to boost its photoactivity depending on the size, morphology, and chemical nature of the plasmonic unit [25]. For example, the mechanism of hot electron injection from the plasmonic unit to the semiconductor conduction band may allow the use of visible light that is not absorbed by a wide-bandgap semiconductor, as widely reported for the TiO₂ photoelectrodes combined with noble metals [26]. Among them, Au and Ag (i.e., alone or alloys), have been mostly considered as possible additives to exploit the plasmonic effects, or to favor charge carrier separation to inhibit recombination, directly contributing to the production of long-lived charges. For instance, Naseri et al. [27] proposed TiO₂ photoanodes decorated with Au–Ag alloy NPs for photoelectrochemical water splitting applications. In particular, photocurrent measurements showed a 30% increase in the presence of alloy NPs as well as a 50% reduction in charge transfer resistance of the electrodes. Other studies reported the use of Au NPs specifically for the treatment of BPA solutions [27–30], focusing on the photoactivity of Au/TiO₂ films, on the plasmonic effect of Au, and on the nature of the support. Very recently, Sreedhar et al. [31] investigated the photoelectrochemical behavior of Au clusters functionalized TiO₂ thin films to explore the role of Au clusters position on charge carrier generation and incident visible light harvesting.

The results demonstrated the great importance of the structure engineering that represents a key point to maximize the light capture and its concentration even in thin semiconductor layers, by increasing the absorption. In fact, the literature, initially focused on solar cells applications, clearly shows that the effect of the noble metal NPs insertion and the consequent operation mechanism of the final structures strongly depend on the particle size and their dispersion within the structure. For instance, the plasmon resonance energy transfer process and the production of hot electrons as well, more likely occur on small particles, while a simple radiation scattering effect is expected on large

particles (>100 nm). Similarly, it was reported that for organic solar cells, the plasmonic effect of small metal NPs can be exploited if the NPs are placed at the interface between two phases where charges separation takes place [32]. Instead, in the case of inorganic solar cells the scattering effect of NPs located away from the p-n junction is exploited [33], even though plasmon effects are also reported in similar cases [34].

As a consequence, the importance of a careful design of the catalyst is evident, which however cannot allow to neglect the analysis of the working mechanism of the structure. In this context, the aim of this work is to investigate the performance of TiO₂ samples with a hierarchical nanostructure, where Au NPs were differently dispersed (i.e., NPs at the bottom or at the top of the TiO₂, as well as integrated TiO₂/Au-NPs assemblies).

The activity of the samples was analyzed by means of photoelectrolysis experiments carried out under neutral pH conditions both towards the possible oxidation of BPA and water molecules. In fact, even if water splitting can not to be particularly favored under such pH conditions, it can be competitive or concomitant with the BPA oxidation.

2. Results

2.1. Structural, Optical, and Electrochemical Properties

Table 1 lists all the investigated samples and their description (i.e., the different distribution of Au NPs).

Table 1. Description and schematic representation of the investigated structures. All samples have a nominal surface of 1 cm × 1 cm and the thickness of the TiO₂ layer was 1000 nm.

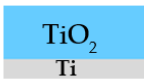




Sample	Description		Au% Vol.
TiO ₂	TiO ₂ film on Ti substrate (Reference)		0
TiO ₂ /Au	Au nanoparticles (NPs) at the bottom of the TiO ₂ film		1
Au/TiO ₂	Au NPs on the top of the TiO ₂ film		1.5
Au/TiO ₂ /Au	Au NPs both at the bottom and on top of the TiO ₂ film		2.5
TiO ₂ -Au	Au-integrated TiO ₂ films		~3.3

Figure 1 shows the morphology of the TiO₂ sample, used as reference (without Au), as well as of the Au loaded samples. All TiO₂ films feature a nanoscale porosity and a hierarchical organization of the nanostructures in ‘nanotrees’ (Figure 1a), which is beneficial for light scattering, electron transport and to obtain large specific surface area values. This kind of structure and the relative properties have been widely discussed in previous works [23,35,36].

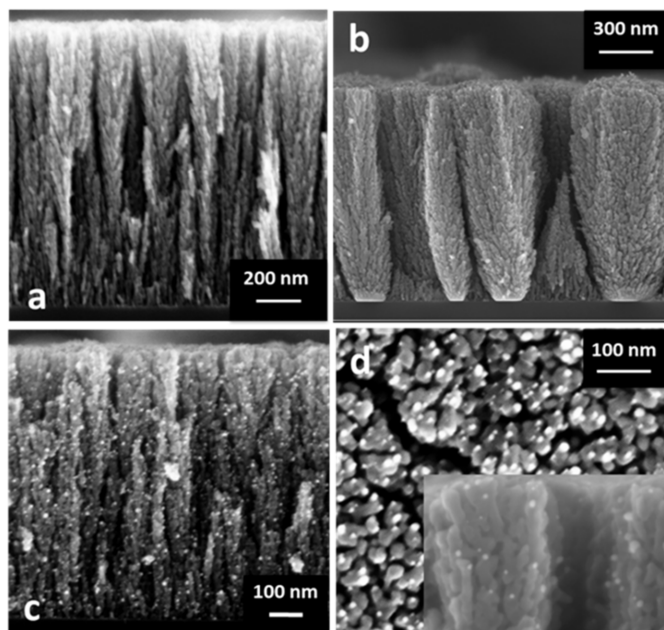


Figure 1. SEM images of (a) reference TiO₂ film (cross section); (b) TiO₂/Au film (cross section); (c) TiO₂-Au film (cross section); (d) the Au/TiO₂ film (top surface; in the inset the film cross section close to the surface shows the penetration of Au NPs).

In detail, the TiO₂/Au sample is characterized by Au NPs at the bottom of the film (Figure 1b) with an average size of 112 ± 44 nm, meant to act as scattering centers in order to induce light diffusion/trapping in the TiO₂ layer [25]. The Au/TiO₂ sample is characterized by NPs deposited on the top surface of the TiO₂ layer, meant to implement plasmonic effects; their average size is 4 ± 1 nm, however nanoparticles as large as ~ 10 nm are present (Figure 1d) [25]. Moreover, the scanning electron microscopy (SEM) image shows that the Au NPs penetrate in the film for a depth of ~ 200 nm. The Au/TiO₂/Au sample combines the features of the previous two films. The TiO₂-Au film is characterized by a nanoscale structure, which is decorated throughout the thickness by Au NPs with an average size of 3 ± 1.5 nm, even though particles as large as 15 nm are present (Figure 1c), as reported in [23]. The amount of Au in the investigated samples is listed in Table 1.

The Au-integrated TiO₂ films are characterized by a strong capability of light scattering, as measured by the haze factor defined in the Experimental section (ratio between diffuse and total transmitted radiation). Table 2 reports the average haze factor for the investigated samples in the visible (wavelength 400–800 nm) and in the near infrared (NIR) region (800–2000 nm). It is clear that the large Au NPs at the bottom of the film (sample TiO₂/Au) act as scattering centers and, while the Au/TiO₂ sample is not characterized by increased light diffusion, the combination of the two Au NP layers has a synergetic effect (sample Au/TiO₂/Au with the highest haze). Small NPs on top or distributed inside the film are instead characterized by a plasmonic absorption feature centered at about 650–700 nm for the TiO₂-Au sample (as reported in [23]), which is also characterized by a large absorption in the whole visible-near infrared (vis-NIR) range (transmittance $<40\%$ in the visible range and $<60\%$ in the NIR); Au NPs at the bottom of the film (~ 100 nm size) are, instead, characterized by plasmonic absorption centered at about 700–800 nm [22].

Table 2. Haze factor % of the samples in two wavelengths.

Sample	Haze Factor (%) 400–800 nm Range	Haze Factor (%) 800–2000 nm Range
Au/TiO ₂ /Au	80	32
TiO ₂ /Au	58	22
TiO ₂	23	Negligible (< 10%)
Au/TiO ₂	16	Negligible (< 10%)
TiO ₂ -Au	11	Negligible (< 10%)

Synthesized samples are submitted to electrochemical characterization in order to investigate their behavior in dark and irradiated conditions. Table 3 reports the values of open circuit voltage (OCV), which give an indication on the equilibrium at the electrode/electrolyte interface. The values measured in the dark at the different samples in neutral and basic solutions are reported. All the values of potential in the text are referred to saturated calomel electrode (SCE).

Table 3. Open circuit voltage (OCV) values measured at different samples, under different pH. The values of OCV at pH 13, calculated by $E = E^0 - 2.3 RT/F \text{pH}$, supposing a Nernstian behavior of the surface, are also reported as a comparison.

Sample	OCV KNO ₃ V/vs SCE	OCV pH 13 V/vs SCE	OCV pH 13 Nernstian V/vs SCE
TiO ₂	−0.14	−0.42	−0.49
TiO ₂ /Au	0.033	−0.11	−0.32
Au/TiO ₂	−0.115	−0.26	−0.47
Au/TiO ₂ /Au	0.022	−0.12	−0.33
TiO ₂ -Au	−0.001	−0.13	−0.35

If the behavior of the reference sample (TiO₂) is considered, a value of −0.14V is measured as OCV in neutral pH, which becomes −0.42 V in basic solution, with a variation very close to the theoretical one, valuable by a linear Nernstian behavior of the surface (last column in Table 3), as it is expected for oxide electrodes [37].

As it can be observed, OCV measured at neutral pH is higher than that expected for TiO₂: lower values, in the range from −0.5 up to −0.85 V, are generally reported as flat band (FB) potential, for TiO₂ bulk, at this pH [38]. Actually, the form of the electrode material (i.e., thin film, single crystal, polycrystalline), its morphology and phase distribution (anatase/rutile) or possible doping are also decisive factors as far as the OCV or FB is concerned.

Regarding the effect of the metal (M), data shown in Table 3 indicate that the presence of Au in the samples, determines a shift of OCV to more positive values, as might be expected, due to the noble character of Au. However, a direct correlation between M loading and OCV is not observed, the extent of the shift being also dependent on the distribution of the NPs in the structure. In fact, the maximum shift (173 mV) is measured for the less M loaded sample (i.e., TiO₂/Au sample) while, rather than at the highest M loaded sample (i.e., TiO₂-Au sample), the minimum shift (25 mV) is measured at Au/TiO₂ sample.

Variation of OCV is also measured (see Figure 2) when samples were submitted to light irradiation, and in the presence of hole scavengers in the electrolyte solution (BPA 50 ppm, in the specific).

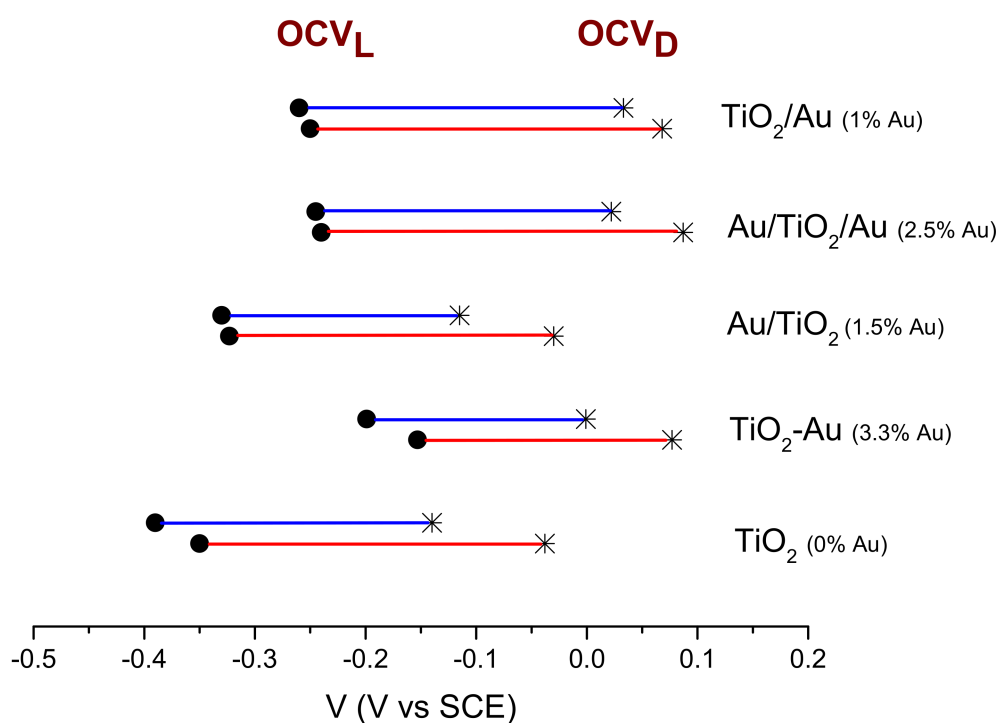


Figure 2. OCV of different samples, under dark (OCV_D: stars) and irradiated (OCV_L: circles) conditions, in supporting electrolyte (blue lines) or in the presence of 50 ppm BPA (red lines).

The n-type semiconductor (SC) behavior is here highlighted: the light determines a shift of the OCV to more negative values. However, as pointed out above, along with the metal loading in the sample, also the NPs distribution and the accessibility of both solution and light, inside the structure, must be considered. To this aim, the open-circuit photopotential (OCP) may give a better indication on the photo-activity of the sample: OCP represents the band-bending change from dark to light irradiation, resulting from photoexcited carriers in n-type SC, flattening the band bending in the depletion region [39]. The final OCP value also depends on the redox couple which is present in the solution. In Figure 3, the trend of OCP measured in supporting electrolyte is compared to that in two different concentrations of BPA: for all the samples, it is a matter of oxidative OCP, whose absolute values are reported. If the effect of the M is concerned, samples Au/TiO₂/Au and TiO₂/Au show a slight increase in OCP in KNO₃, if compared with that measured at TiO₂ sample, which could be in apparent contrast with the relevant values of the OCV. To note, as a consequence of the more positive OCV values measured for the Au/TiO₂/Au and TiO₂/Au samples, a lower efficiency could be expected in terms of OCP, as it is generally obtained in single-crystal systems. However, when the deposited metal film is in the form of small islands or in nanoparticulate form, an enhancement in the photopotential is possible [40,41].

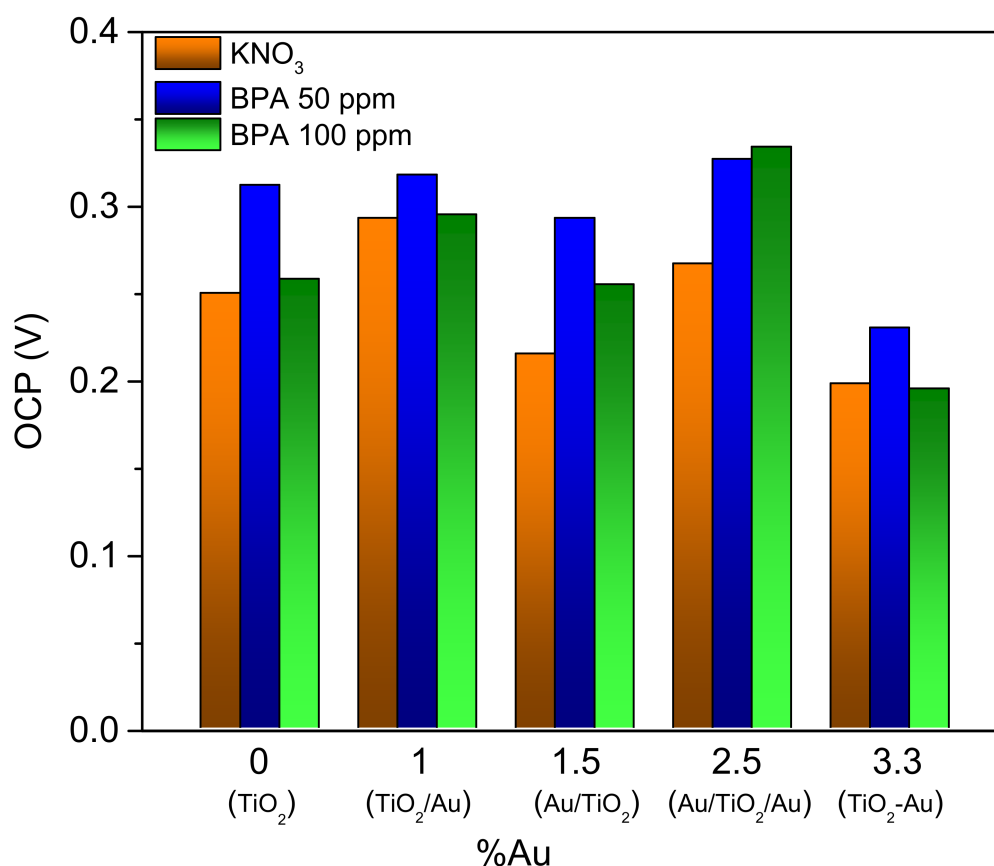


Figure 3. OCP values measured in supporting electrolyte and in two different BPA concentrations at the different samples.

This trend is not observed for the TiO₂-Au and Au /TiO₂ samples, where the M loading makes OCP lower than in TiO₂ sample. At the same time, a not straightforward effect is played by the BPA concentration: on one hand, except for sample TiO₂-Au (OCP = 0.23 V), when 50 ppm BPA are present in the solution the OCP is about 0.3 V, regardless of the M load; on the other hand, lower OCP values are measured at the highest concentration, except for the Au/TiO₂/Au sample.

Table 4 resumes the values of the photocurrent density measured at constant applied potential of 0.5 V, in KNO₃ and in different concentrated BPA solutions, while Figure 4 illustrates the trend of the photocurrents as a function of the different overpotential, evaluated as difference between the applied potential and the OCV_L of the sample.

Table 4. Photocurrent density ($\mu\text{A}/\text{cm}^2$) measured at constant applied potential of 0.5 V vs SCE, in supporting electrolyte and in differently concentrated BPA solutions for the different samples.

	0.1 M KNO ₃	25 ppm BPA	50 ppm BPA	100 ppm BPA
TiO ₂	18	36	50	36
TiO ₂ /Au	32	40	55	36
Au/TiO ₂	25	34	27	39
Au/TiO ₂ /Au	48	44	58	52
TiO ₂ -Au	1.4	1.9	3	1.9

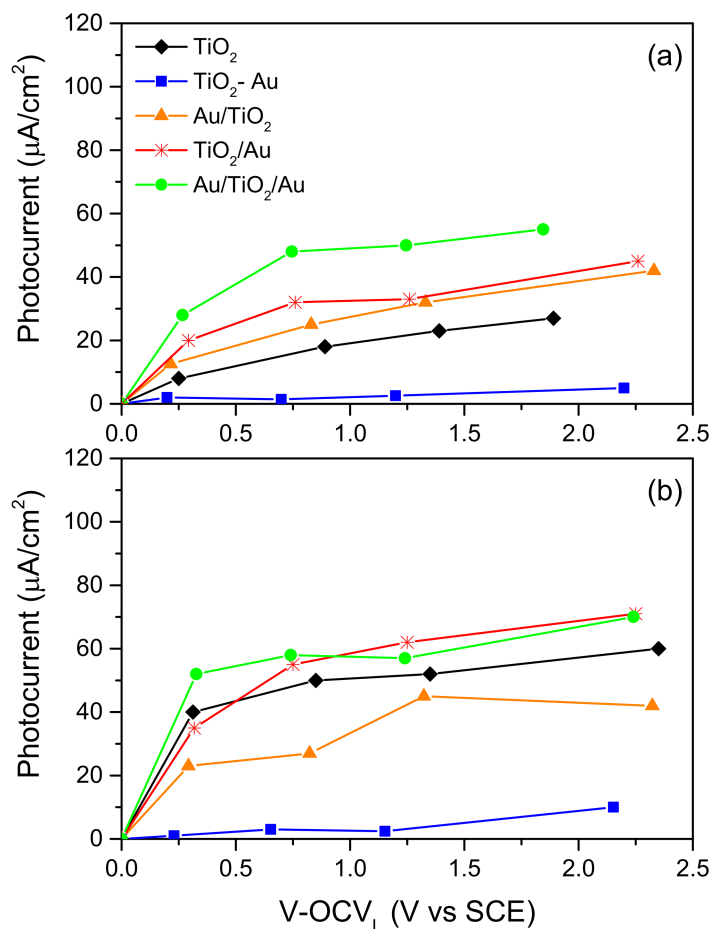


Figure 4. Trend of photocurrent densities as a function of the overpotential with respect to OCV_L , measured in (a) supporting electrolyte and in (b) 50 ppm BPA solution.

Depending on the samples, data appear to be comparable, or even better than those reported in the literature, for analogous electrode materials. As an example, value of photocurrent of $8 \mu\text{A}$ was measured in K_2SO_4 solution at $\text{Au-TiO}_2/\text{ITO}$ [30], while 6 and $30 \mu\text{A}$ were measured at TiO_2/Ti and $\text{Au-TiO}_2/\text{Ti}$ electrodes, respectively, in [29]. More recent work, on nanoroad TiO_2 modified arrays, reports photocurrent of $3.5 \mu\text{A}/\text{cm}^2$ in Na_2SO_4 in the presence of $100 \mu\text{mol}/\text{L}$ BPA [42]. Of note those values were obtained under ultraviolet (UV) irradiation, at which the performance of TiO_2 is expected to be higher than in our irradiation conditions.

In the present case, data indicate a complex effect of NPs inside the structure: except for the $\text{TiO}_2\text{-Au}$ sample, which demonstrated a clearly lower performance than the reference sample, in KNO_3 the positive effect of Au NPs can be assessed in the whole investigated potential range: sample $\text{Au}/\text{TiO}_2/\text{Au}$ appears the most performing in catalyzing the water splitting process. A positive effect of NPs is also measured in the presence of BPA 50 ppm for the $\text{Au}/\text{TiO}_2/\text{Au}$ and TiO_2/Au samples: overpotential being the same, the photocurrents measured on these samples are higher than those measured for the TiO_2 sample. However, in this case, also the performance of Au/TiO_2 is lower than that of the TiO_2 sample. One of the main reasons for the lowest performances of sample $\text{TiO}_2\text{-Au}$ may be the very high load of M, which reduces the porosity and, in turn, the surface area of the sample. Regarding the performance of the Au/TiO_2 sample, SEM analyses, repeated at the end of these experiments, demonstrated a low stability of the sample. Actually, a certain extent of corrosion was detected for all the samples, but for sample Au/TiO_2 , the residual Au content, measured at the end of the experimental campaign, was under the detection limits of the instrument: the low stability of this sample did not allow to perform all the experiments on it.

Among the other possible effects, a conductivity enhancement is expected due to SC/M coupling: the presence of metal NPs should enhance the charge transfer in the structure. The extent of such increase may be deduced by Electrochemical Impedance Spectroscopy (EIS) measurements. Figure 5 shows the Nyquist diagrams obtained by experiments in dark conditions, under -0.5 V of applied potential. This potential was selected in such a way that the space charge of all the n-type semiconductor (SC) samples was in the accumulation regime, so that the majority charge carriers, electrons in the conduction band, could be involved in the charge transfer.

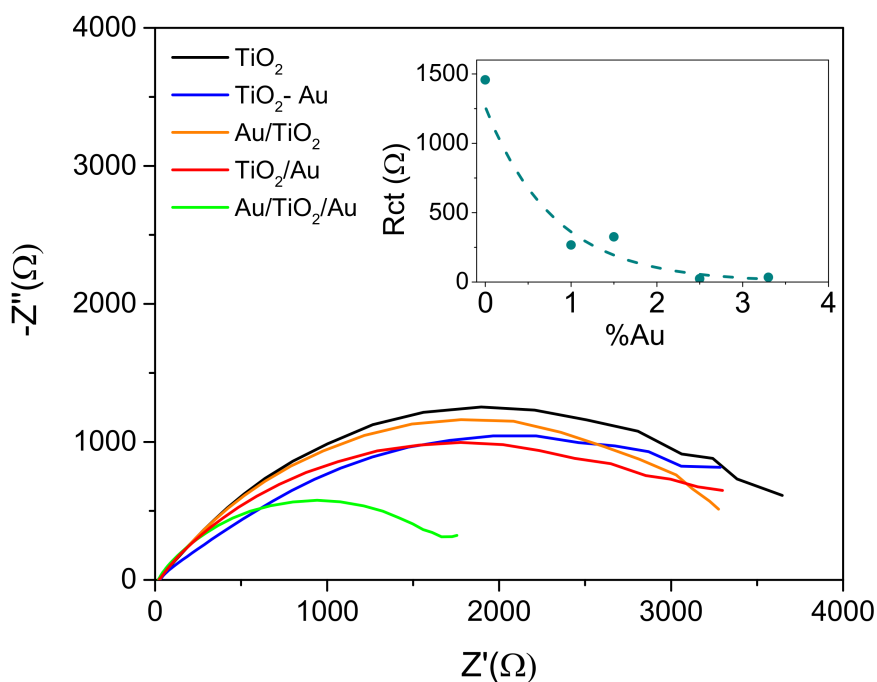


Figure 5. Nyquist plots obtained at $V = -0.5$ V vs SCE, in supporting electrolyte, at different samples. Inset: trend of R_{ct} evaluated by fitting the EIS data with a Randle circuit.

As it can be observed, all the semicircles in Figure 5 tend to be closed on the x-axis: all samples show a good reactivity at this potential, and all the curves related to samples with Au NPs, are under that related to sample TiO_2 , indicating that Au catalyzes the charge transfer process to the solution. The interpretation of these curves with a simple Randle ($R_s(C-R_{ct})$) equivalent circuit, allowed the evaluation of the charge transfer resistance (R_{ct}) for the different samples. The inset in Figure 5 shows that the decrease in R_{ct} is about exponential with the Au load in the samples.

These data are in a nice agreement with the trend of the cyclic voltammeteries (CV) recorded in the dark (Figure 6). In the range of negative potential, similar trends are obtained for the different samples, with a first peak (P1) around -0.7 ± -0.8 V, which should correspond to the $Ti(IV) \rightarrow Ti(III)$ transformation [43], followed by the increase in the negative current due to the H_2 evolution.

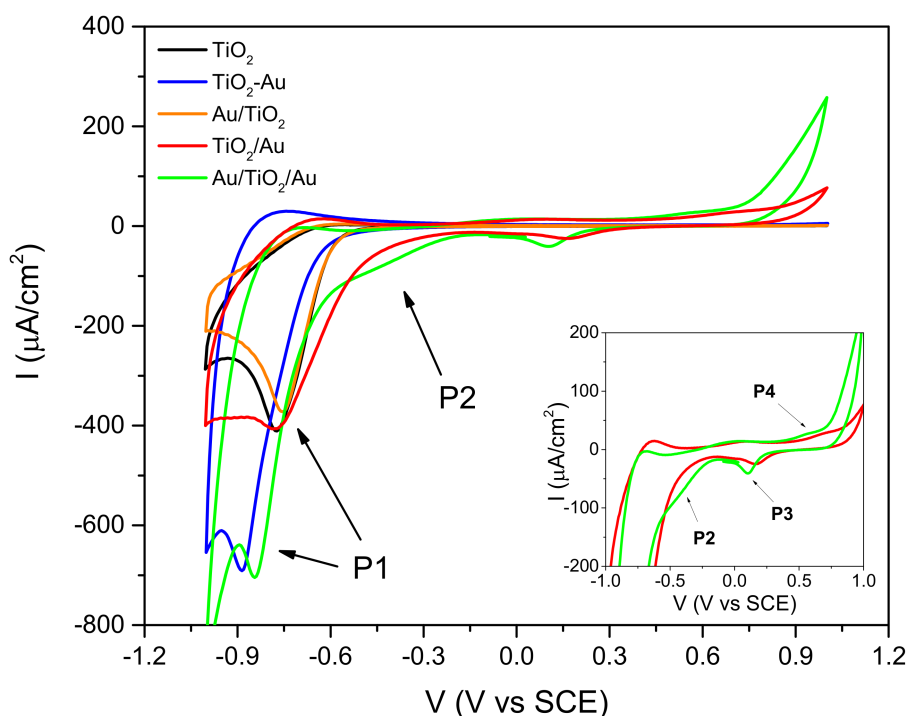


Figure 6. Cyclic Voltammeteries (CV) in supporting electrolyte in dark conditions; the typical peaks of Ti(III)/T(IV) (P1), and of Au redox behavior (P3 and P4) are evidenced in the inset, as well as the wave related to O₂ reduction (P2).

The highest values of current peak P1 are obtained in TiO₂-Au and Au/TiO₂/Au samples: these are the most M loaded and the most conductive samples. On samples Au/TiO₂ and TiO₂/Au, which have a lower M loading, the height of P1 is about half.

In the range of positive potentials, Au/TiO₂/Au is the most active sample for O₂ evolution; the corresponding “wave” related to the O₂ reduction (P2 in the Figure 6) appears around -0.4 V. This wave is also visible at TiO₂/Au sample, but in minor extent, because the O₂ evolution at this sample is of minor extent too. The inset of Figure 6 highlights the redox behavior of Au that is well evident at samples Au/TiO₂/Au and TiO₂/Au: in particular, at these samples the reduction peak of Au at about 0.2 V is coupled with the corresponding oxidation wave (P4), that is observed in the range 0.6 to 1 V, always just before the increase in current, due to O₂ evolution. This redox behavior could result quite different from that generally observed for polycrystalline Au, where two oxidative peaks may be detected. However, as reported in the literature, the voltammetric profiles of the supported nanoparticles differ from those associated with the Au polycrystalline electrode, as the nanoparticles exhibit a single, broad oxidation wave, shifted to more positive potentials, with respect to the two peaks present in the voltammetry of the polycrystalline electrode [44].

However, the redox behavior of Au NPs was not evident in all the samples: for Au-TiO₂ and TiO₂/Au, in which there were no NPs on the bottom, the main effect of NPs was only evidenced in the increased conductivity of the sample (higher P1), while there was no evidence of P3 and P4. Analogous results were obtained by other authors in the literature [31], who found that the voltammetric behavior was very different when Au NPs were deposited under or up the TiO₂ layer: only in the former case CV reported evident peaks related to Au redox reactions, both in the dark and under radiation. This was attributed to the fact that Au clusters grown under the TiO₂ exhibited superior charge carrier generation, separation and transportation than that of TiO₂/Au under visible light.

2.2. Behavior of the Irradiated Samples

Among the several factors determining the photoactivity of a SC material, the concentration of defects plays a crucial role. In the case of reduced TiO₂ materials, oxygen vacancies (VO) and Ti³⁺ sites have been intentionally introduced to obtain a higher photocatalytic/photoelectrochemical activity [45]. Nevertheless, such defects may also act as recombination centers for the photoexcited electron–hole pairs. Thus, to investigate the recombination process in a particular SC structure, the kinetics of the photocurrent decay may be analyzed when, after stabilization in dark conditions, the sample is submitted to irradiation. In such conditions, after an initial spike, in absence of applied potential the current tends to a stationary state: the process follows a first-order kinetics if the decay is only due to a surface recombination [46]. A typical example of the trend in time of the current measured at our samples, as effect of the related photopotential is shown in the inset of Figure 7.

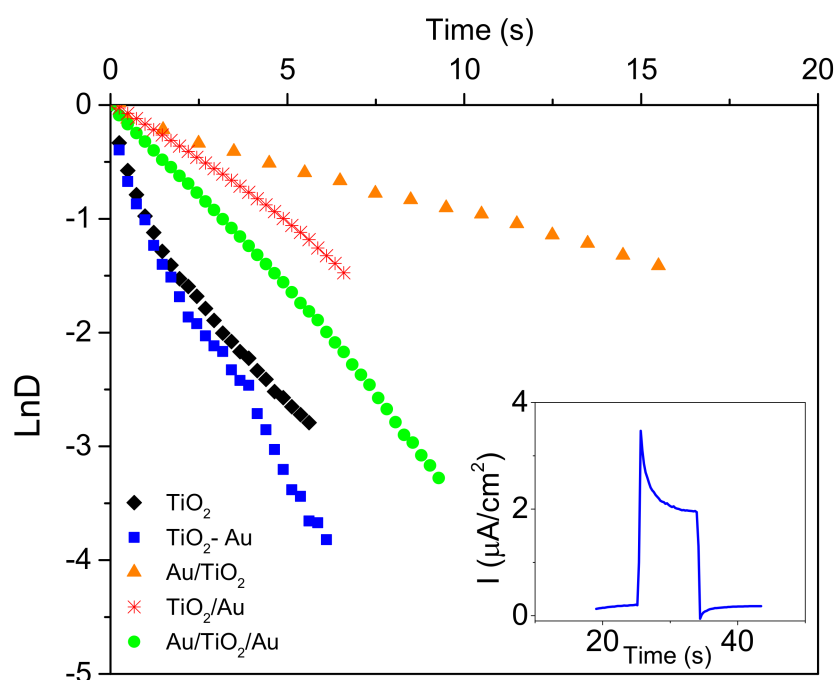


Figure 7. Example of the kinetics of the photocurrent, at TiO₂-Au sample, when the light is suddenly switched on and off.

Two different current transients are observed. The first one, when the light is switched on, describes the initial increase in photocurrent, caused by a separation of the photogenerated electron–hole pairs at the semiconductor/electrolyte interface, followed by an exponential decrease with time. Then, when the light is switched off, a cathodic spike is observed due to the recombination of the conduction band electrons with the holes trapped at the surface [47]. The process can be described by a first order kinetics in the surface concentration of electrons as:

$$D = \exp(-t/\tau) \quad (1)$$

where τ represents the transient time constant, and D takes account of the photocurrent relaxation, defined as:

$$D = (I(t) - I_f)/(I_i - I_f) \quad (2)$$

$I(t)$ is the current at a time t , I_i is the current at $t = 0$, and I_f the stationary current.

Equation (1) can be used to describe both the anodic or the cathodic transients.

In Figure 7 the kinetics of photocurrent relaxation, related to the different samples are compared.

As it can be observed, plots of $\ln D$ vs. time did not always show a linear behavior, indicating that the decay mechanism can be complex. However, in the present case, just to make a qualitative comparison between the different samples, τ was always taken where $\ln D = -1$. The calculated values are resumed in Table 5. The obtained values, of the order of seconds, cannot be representative of charge recombination phenomena only. Actually, these characteristic times are probably affected by electrical transport and electrolyte diffusion phenomena, considering that the porosity of the system, the distribution of defectivities, as well as possible diffusive effects in the pores, may complicate the current decay process.

Table 5. τ values for the different samples evaluated at $\ln D = -1$.

	TiO ₂	TiO ₂ /Au	Au/TiO ₂ /Au	TiO ₂ -Au	Au/TiO ₂
τ (s)	0.97	4.88	3.17	0.97	10.5

However, although the exact indication on the charge recombination time is not derivable from τ , its value can be used to compare the different decay trends: the presence of Au NPs makes the rate of photocurrent decay slower, provided that M loading does not exceed a certain limit. At sample TiO₂-Au the decay is the same as in the original sample, and most of the NPs are probably becoming recombination centres. In this context, the best performance is obtained for the sample Au/TiO₂, but, as already mentioned, this sample demonstrated to be highly unstable.

The effect of light on the CV trends is shown in Figure 8, first with regard to TiO₂ sample.

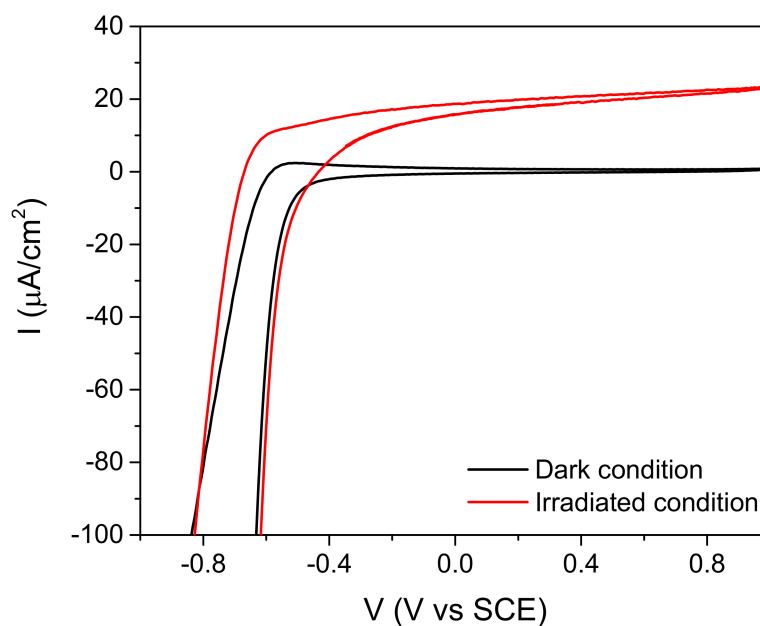


Figure 8. Effect of the irradiation on CV in supporting electrolyte performed at TiO₂ sample.

Attention is focused to the anodic potential range, because, as we expected due to the n-type character of the SC, in this range the effect of the irradiation is more evident.

In Figure 9, the trend of TiO₂ sample is compared with those of the other samples, irradiation conditions being the same.

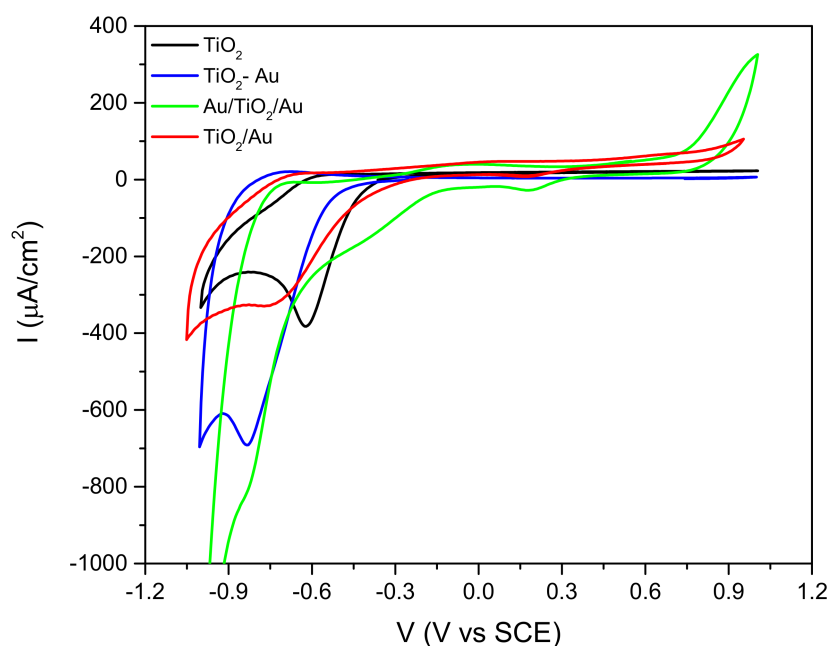


Figure 9. Comparison between CV in supporting electrolyte at different irradiated samples.

Of note is the effect of the irradiation on the O_2 evolution reaction, which is favored for the TiO_2/Au sample and, overall, for the $Au/TiO_2/Au$ sample: for this reason, on this last sample, the corresponding reduction wave P2 is more evident.

2.3. Effect of the Organic Compound on the CV

Specific CV runs performed on the different samples in solutions containing different concentration of BPA, did not show a clear indication of the voltammetric peaks related to the direct oxidation of the organic molecule, at the electrode surface. Nevertheless, the photocurrents recorded in the presence of the organic were higher than those measured in the supporting electrolyte, under almost all the investigated potentials. This may be an indication that oxidation of BPA may occur by means of OH radicals originated from H_2O , by the action of the photogenerated holes. The BPA molecule, acting as OH scavenger, accelerates the separation process of the charges, this in turn gives the increase in the photocurrent.

However, even in the absence of a direct reaction at the electrode surface, the effects of BPA are visible in the CV: the presence of BPA seems to interfere on the redox behavior of the M. For this kind of analysis, we investigated the $Au/TiO_2/Au$ and TiO_2/Au samples, where the redox behavior of the M was more evident: also, they were the most performing systems in terms of photocurrent.

Figure 10a compares the CV obtained in solution with two concentrations of BPA, while Figure 10b compares the trend of CV for the differently M loaded samples in solution with the same concentration of BPA.

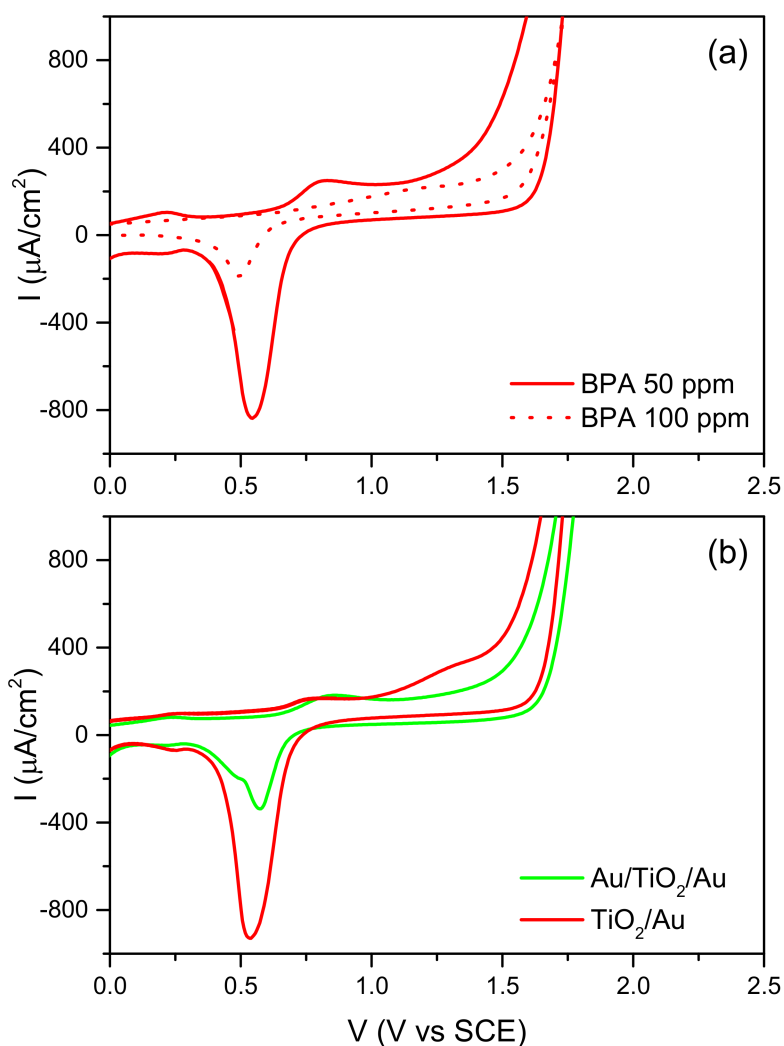


Figure 10. Comparison between the CV obtained at TiO_2/Au sample: (a) in solution with two concentrations of BPA and (b) at samples differently M loaded, in solution with the same concentration of BPA (50 ppm).

The increase in the BPA concentration has two main effects: on one hand, a decrease in the current of the redox peaks (P3 and P4) it is observed, on the other hand, the peaks are more distant one from another, in terms of potential, this indicating a worst and more irreversible charge transfer process with the substrate.

This behavior may indicate that during the CV, in absence of the organic, the photogenerated charges can be available to activate the redox process of the NPs, under the imposed potentials. In particular, during the oxidative scan, the holes may: (i) generate OH radicals from water, or (ii) oxidise Au NPs. In the presence of the organic, BPA molecules act as OH radical scavengers, thus accelerating the path (i) and subtracting holes to the redox process of Au, which is less evident in the CV.

2.4. Analysis of the Working Mechanism of the Structures

From the results presented up to now, it is clear that the behavior of the investigated structures is rather complex: addition of Au NPs interferes not only with the charge transfer to and from the electrolyte, but also with the equilibrium and non-equilibrium interface energetics.

In order to better understand the working mechanism of the electrodes, it can be useful to recall some of the fundamental concepts on SC, how they behave under illumination, and, finally, how they interact with the electrolyte and the solutes in it contained.

From the structural point of view, we are dealing with coupling of SC and M. In the presence of bulk materials, the SC/M interface is expected to behave according to the well-developed theory of SC/metal Schottky contacts [48]. In the specific case, by considering the electronic affinity of TiO₂ equal to 4.5 eV, and a work function (WF) for Au equal to about 5.3 eV [49], coupling of the two materials should lead to a Schottky barrier of 0.8 eV. However, when we deal with nanostructures, the position of the energetic levels may be different: depending on the conditions, and in particular on the morphology of the coupled phases, different values can be calculated for both the Fermi level of the SC, and the WF of the M, which may be affected also by the excess of charge on the NPs [49].

In our specific case, information on the location of the conduction band-edge (CB) can be derived from CV measurements, and, as suggested by the literature [50], we considered the potential of the peak as representative of the energetic level of the CB edge. Thus, a value of 4.4 eV has been calculated from the value of -0.78 V, at which the main peak of TiO₂ appears in the CV of TiO₂ sample.

Regarding the WF of M, we may consider that the OCV values of the samples with Au, were more positive than that of the reference TiO₂ sample (see Figure 2): this may be an indication that the WF of the M was greater than the Fermi level of the SC. When the two materials are contacted, a spontaneous charge transfer occurred from TiO₂ to Au, up to equilibrium leading to the formation of the Schottky barrier. Thus, the presence of Au can be seen as a reservoir of electrons, which are displaced from the CB of the SC: the Fermi level of the SC is lowered, and its potential made more positive by the presence of metal NPs.

When the effect of the irradiation is considered, we cannot neglect that M is present as NPs. In the specific case, optical analyses indicated that for the different samples, depending on the NP dimensions, and on the deep penetration of the Au deposition, plasmonic or scattering effects are originated. In fact, as pointed out in the Introduction, the presence of NPs, more or less distributed in the bulk of the SC or at the interfaces, may strongly enhance the effectiveness of light absorption.

Finally, also the potential of the donor/acceptor redox couples present in the solution must be considered: the Fermi level of the electrons in the CB should remain higher than the energetic level of the acceptor, otherwise it cannot receive electrons at the cathode. At the same time, the level of the holes (h⁺) in the VB of the SC should remain lower than that of the donor to which h⁺ will be transferred.

Accordingly, the scheme shown in Figure 11 illustrates the possible working mechanisms of the examined structures, when irradiated with the whole solar simulated light. Depending on the wavelength of the incident light, different effects could be achieved. The final mechanism should be a combination of the response of the TiO₂ nanostructure, which is sensitive only to a fraction of the wavelengths (UV), and of the Au NP effects (both plasmonic and in terms of charge separation).

Under the fraction of UV radiation, effective on TiO₂:

e⁻ are excited in CB and, assisted by the applied potential, they may:

- (1) go to the cathode (and react with dissolved O₂, or with H₂O to give H₂)
- (2) recombine with h⁺

holes that do not recombine are displaced on the surface and they may:

- (3) react with the electrolyte (oxidising it)
- (4) be transferred to the M (depending on the WF)

holes arriving at the M may:

- (5) be transferred to the electrolyte (in this case, not compatible with the redox level)
- (6) oxidise the M (corrosion).

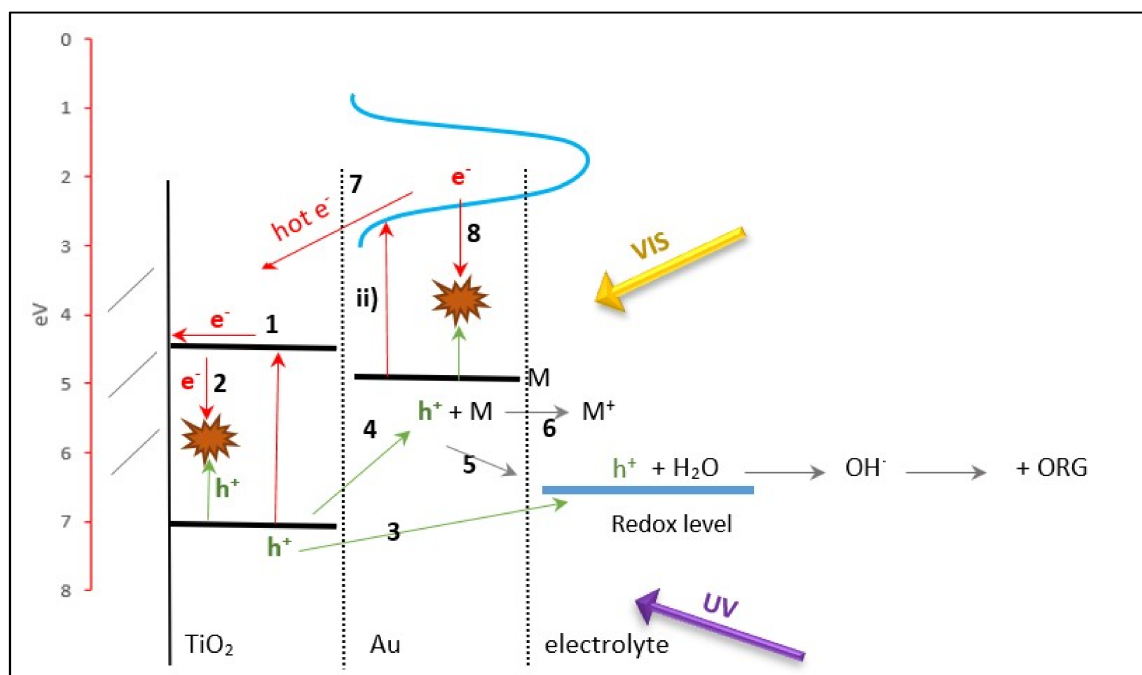


Figure 11. Schematic representation of the energetic levels involved in the charge activation and transfer processes.

The main phenomena related to the illumination of the M nanoparticle can be summarized as:

- (i) scattering effects, able to redistribute radiation in the whole film thickness thus favoring light interaction with the photoanode (this effect is dominated by NPs of great dimensions, not indicated in the scheme),
- (ii) resonant absorption by the localized surface plasmon resonance of the NP (centered in the visible light (VIS) range) with subsequent generation of hot electrons which may:
 - (7) be injected into the CB of the SC (then paths 1, 2)
 - (8) decay and thermalize through electron–electron and electron–phonon scattering.

3. Materials and Methods

The investigated TiO₂ thin films were deposited by Pulsed Laser Deposition (PLD) starting from a 99.9% pure TiO₂ target ablated with Nd:YAG ns laser (Continuum) pulses ($\lambda = 532$ nm, pulse duration 5–7 ns, 10 Hz repetition rate, fluence on the target about 3.5 J/cm²) in a background O₂ atmosphere ($P = 8$ Pa) and with a fixed target-to-substrate distance of 50 mm, at room temperature. The deposition time was adjusted to obtain a nominal thickness for all the films of about 1000 nm. Thermal annealing in air at 500 °C (4 °C/min heating ramp, dwell time 2 h) was employed to induce crystallization to the anatase phase. Crystallinity was verified by Raman spectroscopy (not shown).

Different distribution of Au NPs was achieved, depending on the samples (see Table 1). The TiO₂/Au sample (i.e., the configuration substrate/Au NPs/TiO₂ film) was obtained depositing a TiO₂ film with the above described PLD procedure on a substrate covered with Au NPs obtained by Au thermal evaporation. An Edwards E306 thermal evaporator (Edwards) was employed to deposit a 10 nm Au film, followed by thermal de-wetting (air annealing at 500 °C with 4 °C/min ramp, 2 h dwell) to induce NP growth. The Au/TiO₂ sample (i.e., the configuration substrate/TiO₂ film/Au NPs) was obtained depositing a TiO₂ film by PLD (details above), followed by deposition of Au NPs by PLD, ablating an Au target in 1000 Pa Ar with a laser fluence of 2 J/cm² [22]. The Au/TiO₂/Au sample was obtained by combining the Au/TiO₂ and the TiO₂/Au synthesis procedures. The TiO₂–Au

sample, in which Au NPs are embedded in the nanoporous TiO₂ film, was deposited by PLD ablating a composite Au–TiO₂ target with same ablation parameters as for the pure TiO₂ film, followed by annealing in air at 500 °C (4 °C/min ramp, 2 h dwell) to induce TiO₂ crystallization and Au NPs formation, as described in detail in [23].

All samples characterized by electrochemical techniques were deposited on Ti plate substrates, while selected samples for SEM and optical measurements were deposited on Si (100) and soda lime glass substrates, respectively.

Optical transmittance spectra were evaluated with a UV-vis-NIR PerkinElmer Lambda 1050 spectrophotometer (PerkinElmer, Waltham, Massachusetts, USA) with a 150 mm diameter integrating sphere in the range 250–2000 nm, illuminating the sample from the glass substrate side and normalizing the spectra with respect to glass transmittance. The haze was obtained as the ratio between the diffuse and the total (i.e., diffuse + direct) transmittance intensity.

SEM images of the synthesized samples were acquired using a field emission scanning electron microscope (FEG-SEM, Zeiss Supra 40, Carl Zeiss Microscopy GmbH, Jena, Germany); measurements were also performed, at the end of the experimental campaign, to check the stability of the samples.

Photo-electrochemical characterization of all the samples was performed in an undivided three-electrode cell; the synthesized materials were used as working electrodes, while platinum constituted the counter electrode and SCE was used as reference. The electrodes were connected to a potentiostat-galvanostat (Metrohm Autolab 302N, Metrohm, Herisau, Switzerland), controlled by NOVA software.

The photo-activity of the samples was tested under a light flux provided by a 300W Xe lamp (Lot Oriol, Darmstadt, Germany) equipped with an AM 1.5G filter.

Aqueous solution 0.1 M KNO₃ was used as supporting electrolyte; depending on the experiments, a fixed amount of BPA (25, 50, or 100 ppm) was added to the electrolyte.

For all the cases, the photocurrent was calculated by subtracting the stable value measured in the dark from that obtained under irradiation. Open circuit voltage (OCV) was also monitored, always after 5 minutes of rest, to allow the sample reaching the equilibrium in the solution under the dark (OCV_D) or irradiation (OCV_L) condition imposed. Open Circuit Photopotential (OCP) was also evaluated as the difference between OCV_L–OCV_D in supporting electrolyte or in the presence of organic.

Chronoamperometric tests were performed at different overpotential from the OCP of each sample in both KNO₃ and different concentrated BPA solutions.

Cyclic voltammograms (CV) were recorded in the potential window between –1.1 V and 1.8 V, at 100 mV/s.

Electrochemical impedance spectroscopy (EIS) were performed in the dark, at negative potential, to investigate on the ability of the samples to possible charge transfer process. The investigated frequency range was from 10⁵ Hz to 10^{–1} Hz.

4. Conclusions

Au NPs do not seem to work directly, but we can assess that their presence enhance the ability of the sample to transfer charge with the solvent, and they slow down the decay process of the photocurrent, at least up to a certain load.

If the behavior of the samples is considered in detail, the most performing samples, in both the supporting electrolyte and in the presence of BPA, were the Au/TiO₂/Au and TiO₂/Au samples. On these samples the redox behavior of the M is well evident in the CV, recombination seems slowed down, the current decay is 3–5 times slower than that at the reference sample. On both samples, NPs of great dimensions are present at the bottom under the TiO₂ layer, directly contacting the Ti support. The presence of these NPs at the bottom seems to be the crucial point for the working mechanism of the structure. Thanks to the scattering effects, it is actually possible on these samples to better exploit the radiation, and thus the active sites of the TiO₂ layer.

Measurements for the Au/TiO₂ and Au/TiO₂/Au samples can be useful to interpret the role of the top surface layer of NPs. Considering the smaller dimensions of these NPs, they should be responsible both for possible plasmonic effects and for electron–hole separation, thus leading to reduced recombination. Due to plasmonic effects, localized energetic fields could generate e[−]/h⁺ couples; however, the low stability evidenced for the Au/TiO₂ sample indicates that holes cannot be transferred neither to the electrolyte, nor to the SC, so that they remain in the NPs and oxidize them. However, corrosion seems to be correlated not only to plasmonic effects, but also to the distribution of the NPs. Of note is that the most important corrosion effects are measured, rather than for the TiO₂–Au system, where the plasmonic effects were the most relevant, for the Au/TiO₂/Au and Au/TiO₂ samples, where an upper Au NPs layer is at direct contact with the electrolyte. Maybe the NPs in TiO₂–Au are somehow protected, as they are embedded in the structure. Other works in the literature on similar SC/M coupling, suggested that a protecting layer could be realized in order to avoid corrosion [51].

Finally, the scarce performance of the TiO₂–Au sample could be attributed mainly to a decreased surface area available for the charge transfer with the electrolyte (see [23]). The large content of Au NPs did not result in enhancement of the global performance of the structure. The photocurrent is lower, because the area is lowered. The low value of τ , and the rapid current decay, could indicate that most of the NPs are behaving as recombination centers for the photogenerated charges.

Author Contributions: Conceptualization, S.P. and A.V.; methodology, A.V.; investigation, L.M., E.M.U. and R.M.; writing—original draft preparation, S.P.; writing—review and editing, E.M.U., L.M., M.G., L.M., A.L.B., R.M. and I.N.; sample preparation, structural/optical characterization: M.G., L.M., B.R.B., V.R., C.S.C. and A.L.B.; supervision, A.V. and A.V.; Funding Acquisition, S.P. All the coauthors contributed to the data discussion.

Funding: This research was funded by Fondazione di Sardegna, CRP project F71117000280002 – 2017.

Conflicts of Interest: The authors declare no conflict of interest.

References

1. Careghini, A.; Mastorgio, A.F.; Saponaro, S.; Sezenna, E. Bisphenol A, nonylphenols, benzophenones, and benzotriazoles in soils, groundwater, surface water, sediments, and food: A review. *Environ. Sci. Pollut. Res.* **2015**, *22*, 5711–5741. [CrossRef] [PubMed]
2. Industry Experts. Bisphenol A—A global market overview. 2016. Available online: <http://industry-experts.com/verticals/files/articles/cp021-bisphenol-a-a-global-market-overview.pdf> (accessed on 3 April 2019).
3. Petrie, B.; Lopardo, L.; Proctor, K.; Youdan, J.; Barden, R.; Kasprzyk-Hordern, B. Assessment of bisphenol-A in the urban water cycle. *Sci. Total Environ.* **2019**, *650*, 900–907. [CrossRef] [PubMed]
4. Guerra, P.; Kim, M.; Teslic, S.; Alae, M.; Smyth, S.A. Bisphenol-A removal in various wastewater treatment processes: Operational conditions, mass balance, and optimization. *J. Environ. Manag.* **2015**, *152*, 192–200. [CrossRef] [PubMed]
5. Flint, S.; Markle, T.; Thompson, S.; Wallace, E. Bisphenol A exposure, effects, and policy: A wildlife perspective. *J. Environ. Manag.* **2012**, *104*, 19–34. [CrossRef] [PubMed]
6. Zhan, M.; Yang, X.; Xian, Q.; Kong, L. Photosensitized degradation of bisphenol A involving reactive oxygen species in the presence of humic substances. *Chemosphere* **2006**, *63*, 378–386. [CrossRef]
7. Zhang, C.; Zeng, G.; Yuan, L.; Yu, J.; Li, J.; Huang, G.; Xi, B.; Liu, H. Aerobic degradation of bisphenol A by *Achromobacter xylosoxidans* strain B-16 isolated from compost leachate of municipal solid waste. *Chemosphere* **2007**, *68*, 181–190. [CrossRef]
8. Žerjav, G.; Kaplan, R.; Pintar, A. Catalytic wet air oxidation of bisphenol A aqueous solution in trickle-bed reactor over single TiO₂ polymorphs and their mixtures. *J. Environ. Chem. Eng.* **2018**, *6*, 2148–2158. [CrossRef]
9. Davididou, K.; Nelson, R.; Monteagudo, J.M.; Durán, A.; Expósito, A.J.; Chatzisyneon, E. Photocatalytic degradation of bisphenol-A under UV-LED, blacklight and solar irradiation. *J. Clean. Prod.* **2018**, *203*, 13–21. [CrossRef]

10. Blanco-Vega, M.P.; Guzmán-Mar, J.L.; Villanueva-Rodríguez, M.; Maya-Treviño, L.; Garza-Tovar, L.L.; Hernández-Ramírez, A.; Hinojosa-Reyes, L. Photocatalytic elimination of bisphenol A under visible light using Ni-doped TiO₂ synthesized by microwave assisted sol-gel method. *Mater. Sci. Semicond. Process.* **2017**, *71*, 275–282. [[CrossRef](#)]
11. Repousi, V.; Petala, A.; Frontistis, Z.; Antonopoulou, M.; Konstantinou, I.; Kondarides, D.I.; Mantzavinos, D. Photocatalytic degradation of bisphenol A over Rh/TiO₂ suspensions in different water matrices. *Catal. Today* **2017**, *284*, 59–66. [[CrossRef](#)]
12. Frontistis, Z.; Daskalaki, V.M.; Katsaounis, A.; Poullos, I.; Mantzavinos, D. Electrochemical enhancement of solar photocatalysis: Degradation of endocrine disruptor bisphenol-A on Ti/TiO₂ films. *Water Res.* **2011**, *45*, 2996–3004. [[CrossRef](#)] [[PubMed](#)]
13. Brugnera, M.F.; Rajeshwar, K.; Cardoso, J.C.; Zaroni, M.V.B. Bisphenol A removal from wastewater using self-organized TiO₂ nanotubular array electrodes. *Chemosphere* **2010**, *78*, 569–575. [[CrossRef](#)] [[PubMed](#)]
14. Serra-Pérez, E.; Álvarez-Torrellas, S.; Águeda, V.I.; Delgado, J.A.; Ovejero, G.; García, J. Insights into the removal of bisphenol A by catalytic wet air oxidation upon carbon nanospheres-based catalysts: Key operating parameters, degradation intermediates and reaction pathway. *Appl. Surf. Sci.* **2019**, *473*, 726–737. [[CrossRef](#)]
15. Nguyen, T.B.; Huang, C.P.; Doong, R. Photocatalytic degradation of bisphenol A over a ZnFe₂O₄/TiO₂ nanocomposite under visible light. *Sci. Total Environ.* **2019**, *646*, 745–756. [[CrossRef](#)] [[PubMed](#)]
16. Xu, L.; Yang, L.; Johansson, E.M.J.; Wang, Y.; Jin, P. Photocatalytic activity and mechanism of bisphenol a removal over TiO_{2-x}/rGo nanocomposite driven by visible light. *Chem. Eng. J.* **2018**, *350*, 1043–1055. [[CrossRef](#)]
17. Abdelraheem, W.H.M.; Patil, M.K.; Nadagouda, M.N.; Dionysiou, D.D. Hydrothermal synthesis of photoactive nitrogen- and boron- codoped TiO₂ nanoparticles for the treatment of bisphenol A in wastewater: Synthesis, photocatalytic activity, degradation byproducts and reaction pathways. *Appl. Catal. B* **2019**, *241*, 598–611. [[CrossRef](#)]
18. Mais, L.; Mascia, M.; Palmas, S.; Vacca, A. Photoelectrochemical oxidation of phenol with nanostructured TiO₂ -PANI electrodes under solar light irradiation. *Sep. Purif. Technol.* **2019**, *208*, 153–159. [[CrossRef](#)]
19. Palmas, S.; Castresana, P.A.; Mais, L.; Vacca, A.; Mascia, M.; Ricci, P.C. TiO₂ -WO₃ nanostructured systems for photoelectrochemical applications. *RSC Adv.* **2016**, *6*, 101671–101682. [[CrossRef](#)]
20. Palmas, S.; Mascia, M.; Vacca, A.; Llanos, J.; Mena, E. Analysis of photocurrent and capacitance of TiO₂ nanotube–Polyaniline hybrid composites synthesized through electroreduction of an aryldiazonium salt. *RSC Adv.* **2014**, *4*, 23957–23965. [[CrossRef](#)]
21. Matarrese, R.; Nova, I.; Li Bassi, A.; Casari, C.S.; Russo, V.; Palmas, S. Preparation and optimization of TiO₂ photoanodes fabricated by pulsed laser deposition for photoelectrochemical water splitting. *J. Solid State Electrochem.* **2017**, *21*, 3139–3154. [[CrossRef](#)]
22. Ghidelli, M.; Mascaretti, L.; Bricchi, B.R.; Zapelli, A.; Russo, V.; Casari, C.S.; Li Bassi, A. Engineering plasmonic nanostructured surfaces by pulsed laser deposition. *Appl. Surf. Sci.* **2018**, *434*, 1064–1073. [[CrossRef](#)]
23. Bricchi, B.R.; Ghidelli, M.; Mascaretti, L.; Zapelli, A.; Russo, V.; Casari, C.S.; Terraneo, G.; Alessandri, I.; Ducati, C.; Li Bassi, A. Integration of plasmonic Au nanoparticles in TiO₂ hierarchical structures in a single-step pulsed laser co-deposition. *Mater. Des.* **2018**, *156*, 311–319. [[CrossRef](#)]
24. Atwater, H.A.; Polman, A. Plasmonics for improved photovoltaic devices. *Nat. Mater.* **2010**, *9*, 205–213. [[CrossRef](#)] [[PubMed](#)]
25. Mascaretti, L.; Dutta, A.; Kment, S.; Shalaev, V.M.; Boltasseva, A.; Zboril, R.; Naldoni, A. Plasmon-Enhanced Photoelectrochemical Water Splitting for Efficient Renewable Energy Storage. *Adv. Mater.* **2019**. [[CrossRef](#)] [[PubMed](#)]
26. Pu, Y.; Wang, G.; Chang, K.; Ling, Y.; Lin, Y.; Fitzmorris, B.C.; Liu, C.; Lu, X.; Tong, Y.; Zhang, J.Z.; Hsu, Y.; et al. Au Nanostructure-Decorated TiO₂ Nanowires Exhibiting Photoactivity Across Entire UV-visible Region for Photoelectrochemical Water Splitting. *Nano Lett.* **2013**, *13*, 3817–3823. [[CrossRef](#)] [[PubMed](#)]
27. Naseri, N.; Sangpour, P.; Mousavi, S.H. Applying alloyed metal nanoparticles to enhance solar assisted water splitting. *RSC Adv.* **2014**, *4*, 46697–46703. [[CrossRef](#)]

28. Cojocaru, B.; Andrei, V.; Tudorache, M.; Lin, F.; Cadigan, C.; Richards, R.; Parvulescu, V.I. Enhanced photo-degradation of bisphenol pollutants onto gold-modified photocatalysts. *Catal. Today* **2017**, *284*, 153–159. [CrossRef]
29. Fu, P.; Zhang, P. Uniform dispersion of Au nanoparticles on TiO₂ film via electrostatic self-assembly for photocatalytic degradation of bisphenol A. *Appl. Catal. B* **2010**, *96*, 176–184. [CrossRef]
30. Li, X.Z.; He, C.; Graham, N.; Xiong, Y. Photoelectrocatalytic degradation of bisphenol A in aqueous solution using a Au-TiO₂/ITO film. *J. Appl. Electrochem.* **2005**, *35*, 741–750. [CrossRef]
31. Sreedhar, A.; Reddy, I.N.; Kwon, J.H.; Yi, J.; Sohn, Y.; Gwag, J.S.; Noh, J.-S. Charge carrier generation and control on plasmonic Au clusters functionalized TiO₂ thin films for enhanced visible light water splitting activity. *Ceram. Int.* **2018**, *44*, 18978–18986. [CrossRef]
32. Morfa, A.J.; Rowlen, K.L.; Reilly, T.H.; Romero, M.J.; van de Lagemaat, J. Plasmon-enhanced solar energy conversion in organic bulk heterojunction photovoltaics. *Appl. Phys. Lett.* **2008**, *92*, 013504. [CrossRef]
33. Stuart, H.R.; Hall, D.G. Island size effects in nanoparticle-enhanced photodetectors. *Appl. Phys. Lett.* **1998**, *73*, 3815. [CrossRef]
34. Schaadt, D.M.; Feng, B.; Yu, E.T. Enhanced semiconductor optical absorption via surface plasmon excitation in metal nanoparticles. *Appl. Phys. Lett.* **2005**, *86*, 063106. [CrossRef]
35. Di Fonzo, F.; Casari, C.S.; Russo, V.; Brunella, M.F.; Li Bassi, A.; Bottani, C.E. Hierarchically organized nanostructured TiO₂ for photocatalysis applications. *Nanotechnology* **2009**, *20*, 015604. [CrossRef] [PubMed]
36. Passoni, L.; Ghods, F.; Docampo, P.; Abrusci, A.; Martí-Rujas, J.; Ghidelli, M.; Divitini, G.; Ducati, C.; Binda, M.; Guarnera, S.; et al. Hyperbranched Quasi-1D Nanostructures for Solid-State Dye-Sensitized Solar Cells. *ACS Nano* **2013**, *7*, 10023–10031. [CrossRef] [PubMed]
37. Palmas, S.; Polcaro, A.M.; Rodriguez Ruiz, J.; Da Pozzo, A.; Vacca, A.; Mascia, M.; Delogu, F.; Ricci, P.C. Effect of the mechanical activation on the photoelectrochemical properties of anatase powders. *Int. J. Hydrogen Energy* **2009**, *34*, 9662–9670. [CrossRef]
38. Kavan, L.; Grätzel, M. Highly efficient semiconducting TiO₂ photoelectrodes prepared by aerosol pyrolysis. *Electrochim. Acta* **1995**, *40*, 643–652. [CrossRef]
39. Van de Krol, R.; Grätzel, M. *Photoelectrochemical Hydrogen Production*; Springer: New York, NY, USA, 2012; p. 324. Available online: <https://www.springer.com/us/book/9781461413790> (accessed on 3 April 2019).
40. Nakato, Y.; Tsubomura, H. The Photoelectrochemical Behavior of an n-TiO₂ Electrode Coated with a Thin Metal Film, as Revealed by Measurements of the Potential of the Metal Film. *Isr. J. Chem.* **1982**, *22*, 180–183. [CrossRef]
41. Nakato, Y.; Ueda, K.; Yano, H.; Tsubomura, H. Effect of Microscopic Discontinuity of Metal Overlayers on the Photovoltages in Metal-Coated Semiconductor-Liquid Junction Photoelectrochemical Cells for Efficient Solar Energy Conversion. *J. Phys. Chem.* **1988**, *92*, 2316–2324. [CrossRef]
42. Fan, Z.; Fan, L.; Shuang, S.; Dong, C. Highly sensitive photoelectrochemical sensing of bisphenol A based on zinc phthalocyanine/TiO₂ nanorod arrays. *Talanta* **2012**, *189*, 16–23. [CrossRef]
43. Palmas, S.; Da Pozzo, A.; Mascia, M.; Vacca, A.; Ricci, P.C.; Matarrese, R. On the redox behaviour of glycerol at TiO₂ electrodes. *J. Solid State Electrochem.* **2012**, *16*, 2493–2502. [CrossRef]
44. Rodriguez, P.; Plana, D.; Fermin, D.J.; Koper, M.T.M. New insights into the catalytic activity of gold nanoparticles for CO oxidation in electrochemical media. *J. Catal.* **2014**, *311*, 182–189. [CrossRef]
45. Naldoni, A.; Altomare, M.; Zoppellaro, G.; Liu, N.; Kment, S.; Zboril, R.; Schmuki, P. Photocatalysis with Reduced TiO₂: From Black TiO₂ to Cocatalyst-Free Hydrogen Production. *ACS Catal.* **2019**, *9*, 354–364. [CrossRef] [PubMed]
46. Radecka, M.; Wierzbicka, M.; Komornicki, S.; Rekas, M. Influence of Cr on photoelectrochemical properties of TiO₂ thin films. *Phys. B* **2004**, *348*, 160–168. [CrossRef]
47. Hagfeldt, A.; Lindström, H.; Södergren, S.; Lindquist, S.-E. Photoelectrochemical studies of colloidal TiO₂ films: The effect of oxygen studied by photocurrent transients. *J. Electroanal. Chem.* **1995**, *381*, 39–46. [CrossRef]
48. Rhoderick, E.H.; Willams, R.H. *Metal-Semiconductor Contacts*, 2nd ed.; Oxford University Press: Oxford, UK, 1988; p. 252.
49. Scanlon, M.D.; Peljo, P.; Méndez, M.A.; Smirnov, E.; Girault, H.H. Charging and discharging at the nanoscale: Fermi level equilibration of metallic nanoparticles. *Chem. Sci.* **2015**, *6*, 2705–2720. [CrossRef] [PubMed]

50. Liu, H.; Tang, J.; Kramer, I.J.; Debnath, R.; Koleilat, G.I.; Wang, X.; Fisher, A.; Li, R.; Brzozowski, L.; Levina, L.; et al. Electron acceptor materials engineering in colloidal quantum dot solar cells. *Adv. Mater.* **2011**, *23*, 3832–3837. [[CrossRef](#)] [[PubMed](#)]
51. Awazu, K.; Fujimaki, M.; Rockstuhl, C.; Tominaga, J.; Murakami, H.; Ohki, Y.; Yoshida, N.; Watanabe, T. A Plasmonic Photocatalyst Consisting of Silver Nanoparticles Embedded in Titanium Dioxide. *J. Am. Chem. Soc.* **2008**, *130*, 1676–1680. [[CrossRef](#)]



© 2019 by the authors. Licensee MDPI, Basel, Switzerland. This article is an open access article distributed under the terms and conditions of the Creative Commons Attribution (CC BY) license (<http://creativecommons.org/licenses/by/4.0/>).